



# Freely falling sphere with a rigid rear-side filament

Seungho Choi<sup>1</sup>, Minhyeong Lee<sup>1</sup>, Chris Roh<sup>2</sup> and Daegyoun Kim<sup>1</sup>

<sup>1</sup>Department of Mechanical Engineering, KAIST, Daejeon 34141, Republic of Korea

<sup>2</sup>Department of Biological and Environmental Engineering, Cornell University, Ithaca 14853, USA

**Corresponding author:** Daegyoun Kim, [daegyoun@kaist.ac.kr](mailto:daegyoun@kaist.ac.kr)

(Received 28 August 2024; revised 28 January 2025; accepted 4 March 2025)

In aerodynamic and hydrodynamic devices and locomotive organisms, passive appendages have practical purposes such as drag reduction and flow control. Although these appendages also affect the dynamics of freely falling bodies, underlying principles of their functions remain elusive. We investigate experimentally the dynamics of a falling sphere with a filament appended on its rear side by varying the ratio of filament length to sphere diameter ( $l/D = 0-3.0$ ) and sphere-to-fluid density ratio ( $\rho_s/\rho_f = 1.06-1.36$ ), and maintaining a similar dimensionless moment of inertia ( $I^* \approx 0.96$ ). At the Reynolds number of  $O(10^3)$ , a sphere without any filament exhibits vertical descent. However, the falling of the sphere with a filament is accompanied by periodic horizontal displacements, and the degree of zigzag motion is maximised under specific filament length. The filament induces periodic rotation of the sphere by shifting the centre of mass of the entire model and through the hydrodynamic interaction of the filament with the surrounding fluid. The rotation of the sphere increases the drag force acting on the model, reducing tangential velocity along the trajectory by 14 % compared to a plain sphere. Furthermore, the sphere rotation enhances the lift force normal to the trajectory, extending trajectory length by 5 %. These combined effects improve falling time over a certain vertical distance by 20 % compared to the plain sphere. With increasing sphere density, the effects of the filament on the falling dynamics weaken, because the offset distance between the centre of mass of the model and the geometric centre of the sphere becomes smaller.

**Key words:** flow-structure interactions

## 1. Introduction

Many organisms use passive appendages to improve their locomotion by effectively manipulating the surrounding flow. For instance, elongated tails behind a wing enhance

© The Author(s), 2025. Published by Cambridge University Press. This is an Open Access article, distributed under the terms of the Creative Commons Attribution licence (<https://creativecommons.org/licenses/by/4.0/>), which permits unrestricted re-use, distribution and reproduction, provided the original article is properly cited.

lift and longitudinal stability by modifying the vortical structure in the wake (Park *et al.* 2010). The hairy coating of long appendages enlarges the recirculation bubble formed behind a bluff body, reducing both the drag and the fluctuations in lift (Favier *et al.* 2009). These passive appendages influence the surrounding flow and fluid-dynamic forces, and thus have significant potential for use in engineering applications.

Investigations into the fluid dynamics of passive appendages have mainly considered a splitter plate (a plate attached to the rear side of a bluff body) as the model for passive appendages. A rigid splitter plate attached behind a fixed circular cylinder has been extensively studied in terms of suppressing vortex formation and reducing drag force (e.g. Roshko 1955; Gerrard 1966; Apelt *et al.* 1973; Kwon & Choi 1996; Anderson & Szewczyk 1997; Qiu *et al.* 2014). Compared with a plain cylinder, the splitter plate suppresses vortex shedding in the wake of the cylinder under a uniform flow, and enhances the pressure at the rear of the cylinder, resulting in drag reduction. In addition to rigid splitter plates, flexible splitter plates have been investigated with regard to the fluid force exerted on a fixed circular cylinder and its wake (e.g. Bagheri *et al.* 2012; Lee & You 2013; Wu *et al.* 2014; Mao *et al.* 2022a; Shukla *et al.* 2023). The flexibility and length of the plate determine the hydrodynamic interaction between the splitter plate and the flow, affecting the Strouhal number of vortex shedding, and the drag and lift coefficients of the cylinder. Increasing the number of splitter plates enhances drag reduction for both rigid (Bao & Tao 2013; Abdi *et al.* 2019) and flexible (Niu & Hu 2011; Mao *et al.* 2022b) splitter plates.

In addition to fixed bodies, appendages have been observed to have pronounced effects when attached to the rear side of freely falling bodies. A falling sphere without any appendage follows a straight path at the Reynolds number  $Re (= \bar{v}_z D / \nu) = O(10^2)$ , where  $\bar{v}_z$ ,  $D$  and  $\nu$  are the average vertical velocity, the diameter of the sphere, and the kinematic viscosity of the fluid, respectively (Jenny *et al.* 2004; Veldhuis & Biesheuvel 2007; Horowitz & Williamson 2010; Ern *et al.* 2012). With an increase in  $Re$ , the sphere undergoes a transition to an oblique trajectory. When an elliptic sheet is appended to the rear (upper) side of a falling sphere, the wake of the sphere exerts a fluid force on the sheet, generating a horizontal force to the sphere–sheet model (Lācis *et al.* 2014). Accordingly, the sphere exhibits an oblique falling motion rather than falling vertically. Lācis *et al.* (2017) numerically investigated the effects of the elliptic sheet configuration on the falling dynamics of a sphere. Through a parametric study of various lengths and aspect ratios (the ratio of major axis to minor axis) for the elliptic sheet, the optimal values for maximizing the force in the horizontal direction were identified. In addition to sheet-shaped appendages, the dynamics of falling objects can also be influenced by fibre-shaped appendages. A circular disk, initially inclined as it begins to fall, experiences lateral and angular displacements after release. The multiple bristles attached to the side of the disk mitigate these displacements and allow the disk to fall stably at  $Re = O(10^0)–O(10^2)$ , unlike disks without bristles (Lee *et al.* 2020).

For a body freely falling or rising in a fluid, the translational and rotational dynamics are coupled, causing the body to exhibit different translational dynamics when the rotational dynamics of the body is altered. The rotational motions are largely affected by the moment of inertia and the location of the centre of mass with respect to the geometric centre of the body (Mathai *et al.* 2017; Will & Krug 2021a,b; Assen *et al.* 2024). Previous studies on a falling body with appendages have focused primarily on the translational dynamics of the body, although the coupling of rotational and translational dynamics is critical in determining the trajectory. To elucidate the mutual interaction of a falling body and a rear-side appendage, we experimentally investigate the effects of a single thin filament appendage on the translational and rotational dynamics of a freely falling sphere. Furthermore, although numerous studies have examined the effects of appendages, most

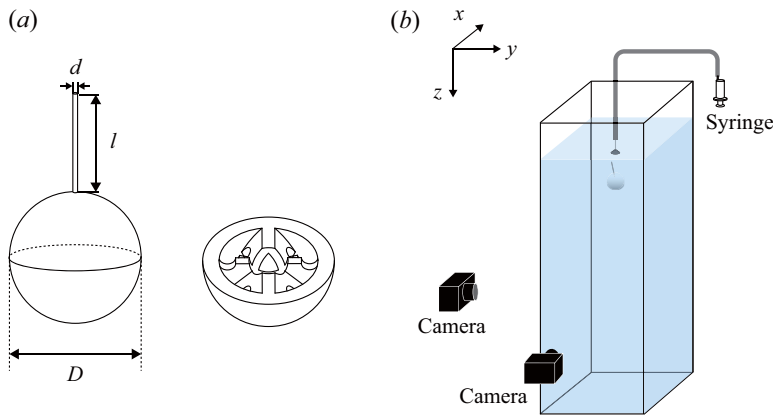


Figure 1. (a) Geometry of a sphere with a filament and internal configuration of the sphere. (b) Schematic of experimental set-up.

have focused on two-dimensional (2-D) objects. The effects of three-dimensional (3-D) filament-shaped appendages attached to a falling object have not been fully understood. Because the falling object possesses higher degrees of freedom compared to a fixed one, the attachment of filament-shaped appendages, even a single appendage, may induce remarkable changes in the trajectory. By varying the filament length and sphere density, the physical mechanisms that determine the falling motions are analysed.

A sphere model with a rear-side filament and experimental methods to measure the 3-D trajectory and rotation of the sphere are described in § 2. In § 3.1, the trajectories and descending times of the sphere are compared for various filament lengths. Section 3.2 examines the role of sphere rotation on the trajectory, with particular emphasis on the forces exerted on the rotating sphere. Section 3.3 discusses the contributions of two mechanisms induced by the attachment of a filament – the shift in the centre of mass and the hydrodynamic interaction of the filament – to the rotational and translational dynamics of the sphere. Subsequently, § 3.4 explores how variations in sphere density determine the falling dynamics. Finally, the main findings of this study are summarised in § 4.

## 2. Experimental set-up

Our experimental model consists of a sphere with a filament attached to its rear (upper) surface (figure 1a). The diameter  $D$  of the spheres in all experimental cases is constant at 16 mm. To maintain almost the same moment of inertia in the sphere while varying its density, the spheres were fabricated to have different internal configurations. Will & Krug (2021b) fabricated spheres with various densities and mass distributions by modifying the internal structure of a shell with a metal ball at its centre. Similarly, we modified the internal structure of two hemispherical shells encompassing a stainless steel ball with mass 0.44 g and diameter 4.76 mm. The hemispherical shells were made from a plastic material (VisiJet M2R-WT, 3D Systems, Inc.) with density  $1.16 \times 10^3 \text{ kg m}^{-3}$  using a 3-D printer (ProJet MJP 2500 Plus, 3D Systems, Inc.). The 3-D printer features layer thickness  $32 \mu\text{m}$  and accuracy  $\pm 0.1 \text{ mm}$  per  $25.4 \text{ mm}$ . The stainless steel ball was positioned at the centre of the sphere, and the hemispherical shells were carefully bonded. The bonded area was sanded to ensure a smooth spherical surface. By modifying the internal configuration of the 3-D printed halves, spheres with different densities ranging from  $\rho_s = 1.06 \times 10^3$  to  $1.36 \times 10^3 \text{ kg m}^{-3}$  have a nearly constant dimensionless moment of inertia  $I^* (= I_s / I_\Gamma) \approx 0.96$ ;

here,  $I_s$  and  $I_\Gamma$  are the moments of inertia of the 3-D printed sphere and a sphere with a uniform density distribution inside and the same mass, respectively. The sphericity of each sphere was estimated by measuring the diameter at different cross-sections with a calliper. The difference between the maximum and minimum diameters was less than 1 % of the desired diameter, confirming that the printed models could be assumed to be ideal spheres.

To attach the thin filament, a small hole of depth 1 mm was made at the apex of the upper hemisphere. The filament, made of acrylonitrile butadiene styrene with density  $\rho_{fil} = 1.08 \times 10^3 \text{ kg m}^{-3}$  and having diameter  $d = 0.5 \text{ mm}$ , was inserted into this hole and carefully aligned to ensure that it remained perpendicular to the surface of the sphere. The mass of the filament was less than 2 % of the sphere mass, having negligible influence on the inertia of the entire model. The filament length  $l$  was varied such that the dimensionless filament length  $l/D$  ranged from 0 (a plain sphere with no filament) to 3.0. The elastic modulus of the filament was measured to be  $2.71 \times 10^3 \text{ MPa}$  at room temperature through tensile test with gauge length 30 mm. All filaments in the range  $l/D = 0\text{--}3.0$  were rigid enough to resist bending by fluid force, as confirmed by the images captured during the falling experiments.

The experiments were conducted in a glass tank of height 160 cm with cross-section  $60 \times 60 \text{ cm}^2$ . The tank was filled with tap water to height 158 cm (figure 1b). Room temperature was maintained at 21 °C, whereupon the water density  $\rho_f$  is  $998 \text{ kg m}^{-3}$  and the kinematic viscosity  $\nu$  is  $0.980 \text{ mm}^2 \text{ s}^{-1}$ . To release the sphere with minimal fluid disturbance, a remotely controlled syringe with a suction cup was used. The syringe restrained the top surface of the sphere to 75 mm below the free surface, then carefully released the sphere. Because the syringe tip was positioned vertically above the centre of the sphere, the filament on the upper surface of the sphere was initially tilted at an angle 15° from the vertical direction. We assessed the effect of this tilting angle on the falling dynamics through a comparison with the same model released at a 0° tilting angle using tweezers, and confirmed that the falling dynamics after the initial transient phase was insensitive to the initial tilting angle. All experimental cases were repeated four times, and each experiment was performed after an interval of at least 15 min to eliminate disturbances in the fluid caused by the previous experiment; 15 min was found to be sufficient according to several trials with different settling times.

To capture 3-D falling motions, two synchronised cameras (VLXT-28M.I, Baumer, Ltd) with resolution  $1920 \times 1464$  pixels were positioned at the front and side of the tank (figure 1b), and the image planes were illuminated using four LED lamps. The falling sphere was filmed at 250 frames per second. Based on the period of sphere motion, the size of the field of view was determined to be 171 mm (in either the  $x$ - or  $y$ -direction)  $\times$  430 mm (in the  $z$ -direction) on the focal plane for each camera. In the images recorded by each camera, the sphere was detected using the Hough circle transform method. The detected sphere centres were used to reconstruct the 3-D position of the sphere, based on calibration using 39 predetermined points in 3-D space (Hedrick 2008).

The investigation of rotational dynamics requires time-resolved measurements for the 3-D orientation of the sphere. To measure the orientation angle of the sphere during the fall, the predetermined black pattern employed by Mathai *et al.* (2016) was marked on the white surface of the sphere. By comparing the filmed image of the sphere and the projection of the analytical pattern onto the 2-D synthetic image, the orientation of the sphere was estimated. The white filament was located on the white part of the sphere to obtain intact images of the black pattern. The orientation measurement could be conducted using a single camera, whereas the position measurement required two cameras. In this study, the results related to the rotational dynamics were obtained from the images captured by one of the two cameras. To validate the accuracy of the orientation

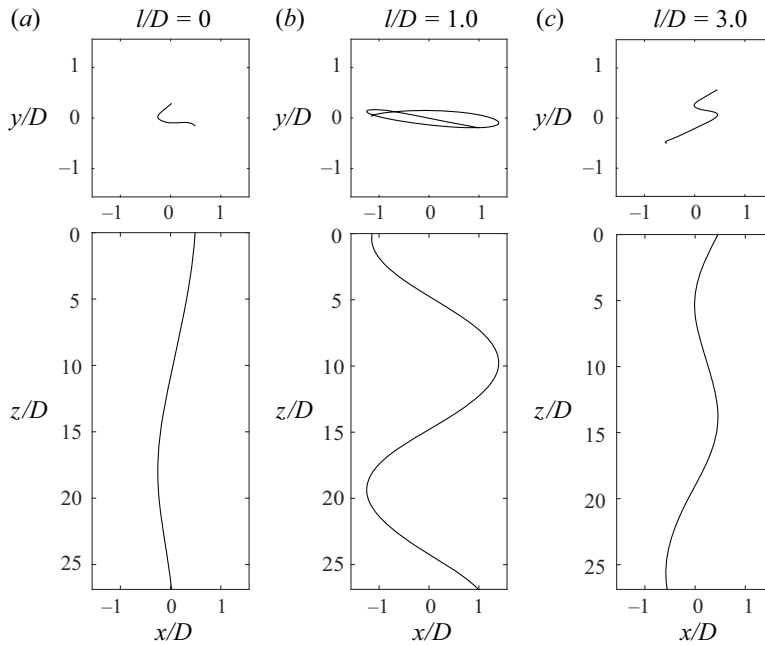


Figure 2. Trajectories of falling spheres with different filament lengths  $l/D$ : (a) 0 (plain sphere), (b) 1.0, and (c) 3.0. Here,  $\rho_s/\rho_f = 1.06$  and  $I^* = 0.967$ , as for all figures and the table in §§ 3.1–3.3. The upper and lower panels are top and side views, respectively, and the  $z$ -axis aligns with the gravitational direction. See supplementary movie 1.

measurement, the sphere was rotated by a predetermined angle while its centre was fixed. The measured angular difference between the initial and final orientations was then compared with this predetermined angle. Small errors between the predetermined and measured angles confirm that the orientation measurement method used in this study is reliable for analysing the sphere’s rotational dynamics. Detailed procedure and validation of the orientation measurement are explained in Appendix A.

### 3. Results and discussion

#### 3.1. Characteristics of zigzag trajectory

When a filament is attached to the upper side of a sphere falling in a quiescent fluid, the moment of inertia of the model increases, and its centre of mass shifts upwards from the geometric centre of the sphere alone. These altered properties of the sphere induce different hydrodynamic interactions between the sphere and fluid compared with those of a plain sphere with no filament, resulting in distinct falling motions. In this subsection, we analyse the effects of the rear-side filament on the translational dynamics of the falling sphere. The filament length  $l$ , which is made dimensionless using the sphere diameter  $D$ , is the major parameter in this study, and the sphere exhibits distinct trajectories depending on  $l/D$  (see figure 2 and supplementary movie 1). To focus on the effects of  $l/D$ , the density ratio of the sphere to the fluid is fixed at  $\rho_s/\rho_f = 1.06$  for all experimental results in §§ 3.1–3.3, regardless of the filament length; the corresponding dimensionless moment of inertia  $I^*$  of the sphere is constant at 0.967.

The falling mode of a plain sphere is determined by the Reynolds number  $Re = \bar{v}_z D/\nu$  and the density ratio  $\rho_s/\rho_f$ , where  $\bar{v}_z$  is the average vertical velocity of the sphere

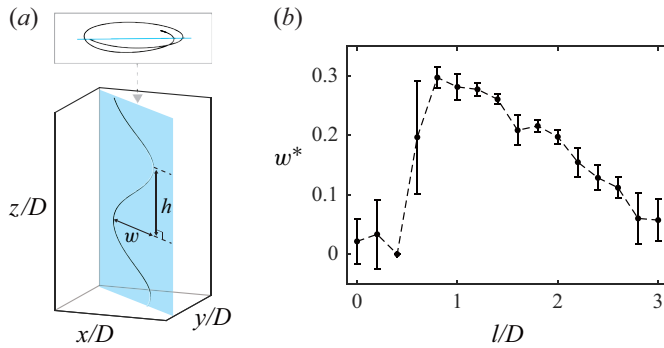


Figure 3. (a) Description of 2-D trajectory plane (blue) and length parameters to represent zigzag trajectory. The upper inset shows the top view of the trajectory. (b) Degree of zigzag motion  $w^*$ , with respect to  $l/D$ . The error bar represents the standard deviation from the mean for each measurement point.

(Horowitz & Williamson 2010). For our plain sphere,  $Re = 2.71 \times 10^3$  and  $\rho_s/\rho_f = 1.06$ . According to the previous study (Horowitz & Williamson 2010), these values of  $Re$  and  $\rho_s/\rho_f$  correspond to the region where the sphere falls vertically. In figure 2(a), the falling trajectory of the plain sphere ( $l/D = 0$ ) is predominantly rectilinear, with a slight horizontal deviation; the scale of the  $z$ -axis differs from that of the other axes in the figure. The maximum horizontal distance between any two points projected onto the  $xy$ -plane is  $0.77D$ , which is sufficiently small compared with the vertical travel distance, thus the motion can be classified as vertical falling. The fluid domain depicted in figure 2 is far from the release point controlled by the syringe, so the trajectory does not include the initial transient phase immediately after release;  $z/D = 0$  in the figure is located 900 mm below the syringe tip. For our plain sphere,  $Re$  generally belongs to the intermediate regime between laminar and turbulent flows, and the minor horizontal displacement in figure 2(a) might be induced by flow instability around the sphere. However, the amplitude of the horizontal displacement is so small that the trajectory of our plain sphere can be considered to be vertical. Although the  $Re$  values of the models in this section range from  $2.31 \times 10^3$  to  $2.71 \times 10^3$ , the falling sphere exhibits a distinct zigzag motion for an intermediate filament length  $l/D \approx 1.0$ , instead of the almost rectilinear motion observed for  $l/D = 0$  (figure 2b). This zigzag trajectory is not completely within a 2-D plane. In other words, the sphere with the zigzag motion moves periodically in both the major direction of maximum horizontal displacement and the minor direction normal to the major direction (upper panel of figure 2b).

To quantify the degree of zigzag motion, a 2-D trajectory plane is first defined, on which the horizontal amplitude of the zigzag motion is maximum along the direction parallel to the plane; see the blue plane in figure 3(a). The 2-D trajectory plane is constructed by fitting all positions of the trajectory onto the plane using the least squares method. During the zigzag motion, the sphere periodically reaches peak positions at which the horizontal movement along the major direction reverses. The horizontal displacement between two successive peak positions along the direction parallel to the trajectory plane is denoted as  $w$  (figure 3a). The horizontal displacement in the minor direction has a similar magnitude, regardless of the filament length. The filament length has a pronounced effect on the horizontal displacement in the major direction. Therefore, only the horizontal displacement along the major direction is considered for the degree of zigzag motion. The trajectory height  $h$  is the distance between two successive peak positions along the direction perpendicular to the direction defining  $w$ , and parallel to the trajectory plane (figure 3a), indicating how quickly the direction of the trajectory changes.

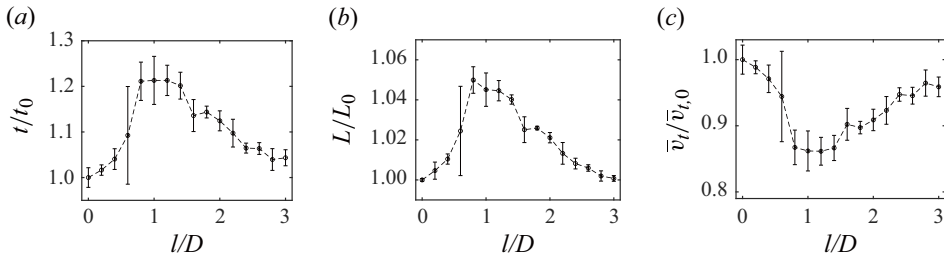


Figure 4. (a) Falling time  $t/t_0$ , (b) trajectory length  $L/L_0$ , and (c) average tangential velocity  $\bar{v}_t/\bar{v}_{t,0}$  with respect to  $l/D$ .

These two parameters are the basic parameters to quantify the zigzag motion. The average horizontal displacement in the major direction,  $w_{avg}$ , is made dimensionless using the average trajectory height  $h_{avg}$ :  $w^* = w_{avg}/h_{avg}$ . Here,  $w_{avg}$  and  $h_{avg}$  are the averages of  $w$  and  $h$ , respectively, calculated over multiple periods within a single experimental trial. Rather than using  $w_{avg}$  and  $h_{avg}$  separately, we present the zigzag motion using a single dimensionless parameter  $w^*$ , which effectively characterises the intensity of zigzag motion by quantifying the sphere’s horizontal displacement relative to the distance over which the sphere completes half a cycle of the zigzag motion.

For small  $l/D$  (typically  $\leq 0.4$ ),  $w^*$  is close to zero, which indicates that the sphere exhibits almost no zigzag motion (figure 3b). However, when  $l/D$  exceeds 0.4,  $w^*$  increases remarkably until  $l/D = 0.8$  with the emergence of a distinct zigzag motion. In figure 3(b), the spread of measured values is represented by an error bar, which indicates the standard deviation above and below the mean; throughout this study, all error bars denote the standard deviation from the mean at each measurement point. The large standard deviation of the experimental results for  $l/D = 0.6$  signifies a transition regime from non-zigzag to zigzag motion. In this regime, both the zigzag and non-zigzag motions are observed in the experimental trials. As  $l/D$  increases from 0.8, the zigzag motion becomes weaker, with a smaller value of  $w^*$ . For the sphere with a long filament ( $l/D \approx 3.0$ ), the zigzag path almost disappears, as depicted in figure 2(c). Interestingly,  $w_{avg}$  remains nearly constant for  $l/D = 0.6$  and 1.2, with  $w_{avg}/D = 2.43$  and 2.44, respectively. Despite these similar  $w_{avg}/D$  values,  $w^*$  for  $l/D = 0.6$  is much smaller than that for  $l/D = 1.2$  due to the greater average trajectory height  $h_{avg}$ , which exemplifies that  $w_{avg}/D$  alone does not successfully quantify the degree of zigzag motion, and  $w^*$  should be employed as a primary parameter.

Because the filament displaces the sphere horizontally, it also affects the vertical falling speed of the sphere. Here, the falling time  $t$  required for the sphere to move from  $z/D = 0$  to  $z/D = 26.9$  is made dimensionless using the falling time of the plain sphere,  $t_0$ ; the  $z$ -axis is positive downwards, and hereafter the subscript 0 denotes the result of the plain sphere ( $l/D = 0$ ). All experimental data obtained in this study are measured between  $z/D = 0$  and  $z/D = 26.9$  (top and bottom of the 3-D trajectory domain, respectively). The value of  $t/t_0$  is greater than unity for all spheres with a filament, which means that when a filament of any length is attached, the sphere takes a longer time to fall a certain vertical distance than the plain sphere (figure 4a). As  $l/D$  increases from 0 to 0.8,  $t/t_0$  increases, reaching a plateau near  $t/t_0 = 1.2$  within the range  $l/D = 0.8–1.4$ . Beyond this range,  $t/t_0$  decreases with increasing  $l/D$ . The trend of  $w^*$  versus  $l/D$  in figure 3(b) is similar to that of  $t/t_0$ . The falling time associated with a strong zigzag motion tends to be greater than that with a weak zigzag motion.

When the sphere follows the zigzag trajectory, the total distance travelled by the sphere (i.e. trajectory length) increases from the vertical falling distance, which contributes to

the prolongation of the falling time. In addition to the extension of the trajectory length, the filament changes the tangential velocity of the sphere along the trajectory, which also affects the falling time. The trajectory length  $L$  and average tangential velocity  $\bar{v}_t$  along the trajectory between  $z/D = 0$  and  $z/D = 26.9$  are computed to examine their effects on the falling time. The trajectory length divided by that of the plain sphere,  $L/L_0$ , exhibits a correlation with  $t/t_0$ :  $L/L_0$  grows from  $l/D = 0$  to  $l/D = 0.8$ , and thereafter declines from  $l/D = 0.8$  to  $l/D = 3.0$  (figure 4*b*). That is, the extended trajectory length owing to the filament contributes to the prolonged falling time.

In contrast to the trajectory length, the ratio of the average tangential velocity to that of the plain sphere,  $\bar{v}_t/\bar{v}_{t,0}$ , exhibits the inverse trend to that of  $t/t_0$  (figure 4*c*). The upper bar denotes the time-averaged value of the results obtained during the experimental trial. The minimum value of  $\bar{v}_t/\bar{v}_{t,0}$  reaches 0.86 near  $l/D = 0.8$  and 1.4, and the ratio approaches unity almost monotonically as  $l/D$  decreases below 0.8 or increases beyond 1.4. This result indicates that the attachment of a filament induces the falling dynamics that differ from those expected based on previous investigations on the effects of rear-side appendages. For instance, previous studies focused primarily on the role of appendages on drag reduction for fixed bluff bodies in 2-D configurations (Roshko 1955; Apelt *et al.* 1973; Kwon & Choi 1996; Anderson & Szewczyk 1997; Qiu *et al.* 2014). If the same mechanism of these appendages was applicable to our experimental model, then one would expect an increase in tangential velocity because of drag reduction. However, this study reveals an unexpected result. The 2-D appendages in the previous studies split the wake of the fixed bluff body, thereby reducing the drag coefficient. By contrast, our sphere is free to move, and the filament does not split the wake in the same manner due to its small cross-sectional area relative to the sphere's wake. Thus the mechanism by which the filament-shaped appendage affects the freely falling sphere is fundamentally different from how a 2-D appendage influences a fixed bluff body. Indeed, for all filament lengths, the tangential velocity of the sphere with the filament is lower than that of the plain sphere. Furthermore, the reduction in  $\bar{v}_t$  is pronounced when the zigzag pattern becomes dominant with greater  $w^*$  (figure 3*b*).

The attachment of a filament to the sphere results in an extended trajectory and slower movement, leading to prolonged falling time compared to the plain sphere. While changes in both the trajectory length and tangential velocity affect the falling time, the effect of reducing the tangential velocity is more significant than that of elongating the trajectory length. For example,  $\bar{v}_t$  decreases by a maximum of 14 % from  $\bar{v}_{t,0}$ , while  $L$  increases by a maximum of 5% from  $L_0$ , according to figures 4(*b*) and 4(*c*). To elaborate the trend of the tangential velocity along the zigzag path, the rotational motion of the sphere and its coupling with the translational motion are discussed in § 3.2.

### 3.2. Mechanism of sphere rotation

The rotational dynamics of the sphere with a filament is now analysed in terms of the angular velocity of the sphere and the orientation of the filament. To represent the angular velocity as a single parameter, instead of expressing it with three Cartesian components, the angular velocity vector of the sphere,  $\boldsymbol{\omega}$ , is obtained from the axis-angle notation (Zimmermann *et al.* 2011; Mathai *et al.* 2016). During the falling process, the rotation of the sphere exhibiting a zigzag translational motion is mostly confined in two opposing directions that share a single axis, which are depicted as red and blue arrows on the top sphere of figure 5(*a*). This rotation axis is normal to the 2-D trajectory plane described in § 3.1. The unit normal vector of the trajectory plane,  $\boldsymbol{n}$ , is defined as the vector perpendicular to this plane with a positive  $x$ -component in the global coordinate system.

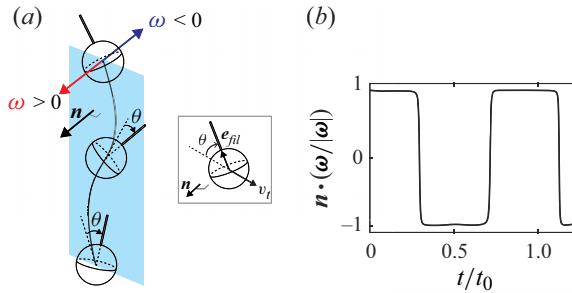


Figure 5. (a) Sign convention of angular velocity  $\boldsymbol{\omega}$  and definition of filament angle  $\theta$ . (b) Inner product of unit angular velocity vector  $\boldsymbol{\omega}/|\boldsymbol{\omega}|$  and unit normal vector of the trajectory plane,  $\mathbf{n}$ , for  $l/D = 1.0$ .

As a representative result, the inner product of the unit angular velocity vector  $\boldsymbol{\omega}/|\boldsymbol{\omega}|$  and the unit normal vector  $\mathbf{n}$  is presented in figure 5(b) for the case of  $l/D = 1.0$ , which undergoes a strong zigzag motion. The value of  $\mathbf{n} \cdot (\boldsymbol{\omega}/|\boldsymbol{\omega}|)$  is close to either 1 or  $-1$ , indicating that the rotation axis of the sphere is almost aligned with the normal vector of the trajectory plane during the fall. In contrast to cases with a distinct zigzag motion, the cases with a subtle zigzag motion have weaker alignment, thus the transition of  $\mathbf{n} \cdot (\boldsymbol{\omega}/|\boldsymbol{\omega}|)$  between 1 and  $-1$  occurs over a longer time, resulting in a smoother plot.

Considering the sign of the rotation direction, the angular velocity of the sphere,  $\omega$ , is defined as

$$\omega = \text{sgn}(\boldsymbol{\omega} \cdot \mathbf{n}) |\boldsymbol{\omega}|, \quad (3.1)$$

where  $\text{sgn}$  is the signum function. To characterise the behaviour of the filament with respect to the sphere motion, the filament angle  $\theta$  is introduced as the angle between  $-\mathbf{v}_t$  (the negative value of the tangential velocity vector along the trajectory) and  $\mathbf{e}_{fil}$  (the vector from the sphere centre to the filament), as shown in figure 5(a):

$$\theta = \text{sgn} \left[ \{ \mathbf{e}_{fil} \times (-\mathbf{v}_t) \} \cdot \mathbf{n} \right] |\theta|. \quad (3.2)$$

In this study,  $\omega$  and  $\theta$  represent fundamentally different quantities, and  $\omega$  should not be interpreted as the time derivative of  $\theta$ . This distinction arises because the filament deviates from the trajectory plane, thus  $\mathbf{e}_{fil}$  is not parallel to this plane.

The time series of the filament angle  $\theta$  and the sphere angular velocity ratio  $\omega/|\omega_0|$  for  $l/D = 1.0$  are presented in figures 6(a) and 6(b), respectively. Here,  $|\omega_0|$  is the time-averaged magnitude of the plain sphere's angular velocity between  $z/D = 0$  and  $z/D = 26.9$ . For a falling plain sphere of the same density and Reynolds number as our model, two vortex rings appear in the wake during one period of wake formation (Horowitz & Williamson 2010). In the present experiment, the plain sphere exhibits slight rotation due to interaction with the unsteady wake, having non-zero  $|\omega_0|$ . Despite its small magnitude,  $|\omega_0|$  is used as the denominator in the angular velocity ratio to express the magnitude of the angular velocity of the sphere with a filament relative to that of the plain sphere. For five representative instants during the fall (red dots in the figures), their corresponding positions are marked along the 3-D falling trajectory in figure 6(c). Positions 2 and 4 are the peak positions at which the horizontal displacement of the sphere attains a local maximum. Positions 1, 3 and 5 are determined as the locations that make the vertical distances between neighbouring positions equal.

Although  $\omega$  is not the time derivative of  $\theta$  by definition (as mentioned above), their time series in figures 6(a) and 6(b) show some correlation. Specifically,  $\omega$  approaches zero and changes its sign when  $\theta$  reaches its local maximum or minimum value, and  $\theta$  approaches

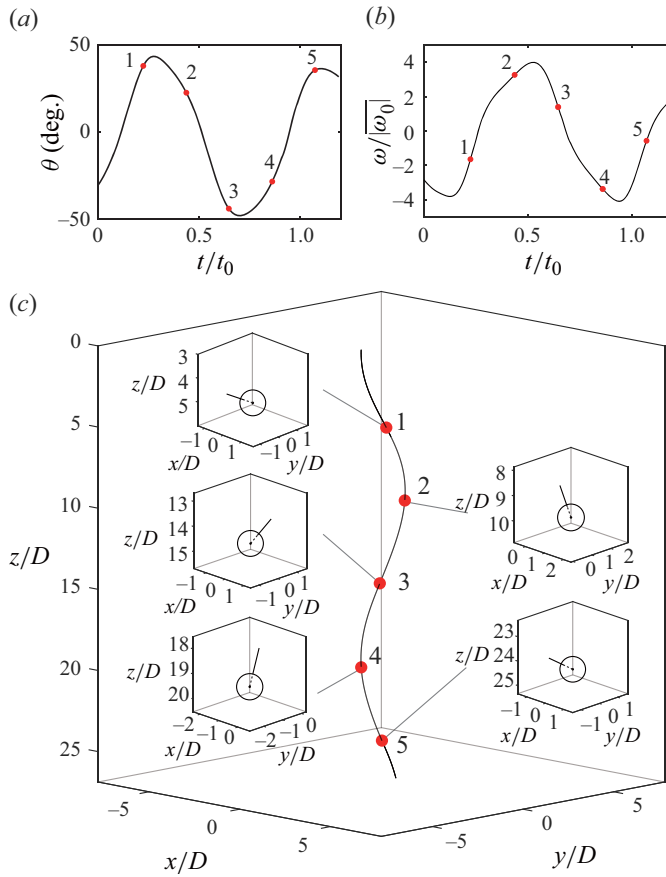


Figure 6. Time histories of (a) filament angle  $\theta$  and (b) sphere angular velocity  $\omega/|\omega_0|$  for  $l/D = 1.0$ . (c) The 3-D trajectory corresponding to (a) and (b). The insets (c) depict the orientation of the filament at each position represented by the red dots.

zero and changes its sign when  $\omega$  reaches its local extreme value. This is because the rotation axis of the sphere almost aligns with  $\mathbf{n}$  in this case. As explained in § 3.1, the translational motion of the sphere is dominant in the major direction over the minor direction. The alignment between the rotation axis and the normal vector of the trajectory plane constructed based on the translational motion suggests that the translational motion of the sphere is strongly coupled with its rotational motion. Pronounced alignment is observed in cases with a strong zigzag motion (e.g.  $l/D = 1.0$  in figure 6). In contrast, for cases with a weak or negligible zigzag motion, no clear correlation is observed between  $\theta$  and  $\omega$ .

The relationship between the translational and rotational motions can also be identified from the degree of zigzag motion and the angular velocity of the sphere. To reveal the effects of the filament length on the rotational dynamics, the magnitude of the sphere angular velocity,  $|\overline{\omega}|$  averaged between  $z/D = 0$  and  $z/D = 26.9$ , with respect to  $l/D$  is shown in figure 7(a). All spheres with a filament rotate faster than the plain sphere;  $|\overline{\omega}|$  increases from  $l/D = 0$  to  $l/D = 0.8$ , then decreases as  $l/D$  increases beyond 0.8. The trend of  $|\overline{\omega}|$  is similar to that of  $w^*$  in figure 3(b), indicating that the enhanced rotation of the sphere is correlated with the strong zigzag motion. In contrast, the maximum magnitude of the filament angle,  $|\theta|_{max}$ , exhibits a similar trend to  $|\overline{\omega}|$  for  $l/D \geq 0.8$ , but a

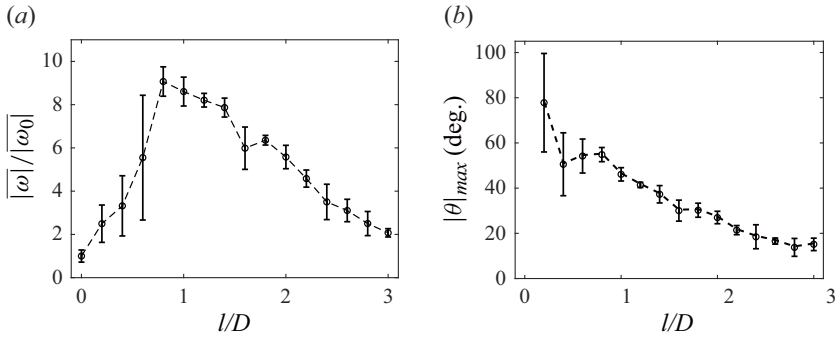


Figure 7. (a) Average magnitude of sphere angular velocity  $|\omega|/|\omega_0|$ . (b) Maximum magnitude of filament angle  $|\theta|_{max}$  for different filament lengths.

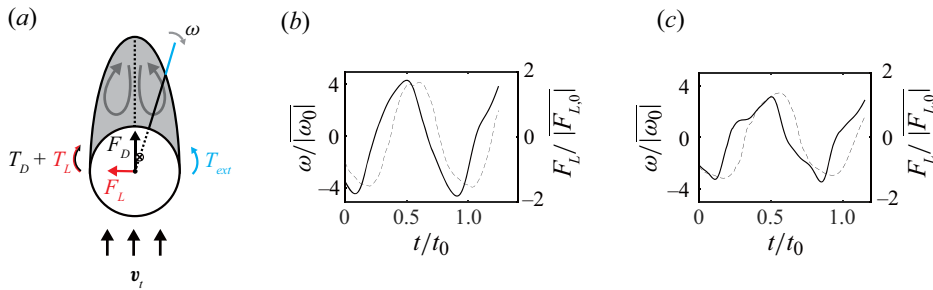


Figure 8. (a) Schematic illustrating a wake region (grey) and the components of forces and torques acting on the model. The reference frame is fixed with the sphere. Time histories of sphere angular velocity  $\omega$  (solid line) and lift force  $F_L$  (dashed line) for (b)  $l/D = 1.0$  and (c)  $l/D = 2.0$ .

different trend for  $l/D < 0.8$  (figure 7b). For  $l/D \geq 0.8$ , the sphere with a longer filament rotates with a smaller amplitude of the filament angle. However, when  $l/D$  is less than 0.8,  $|\theta|_{max}$  exhibits significant scatter, despite having large values. A large standard deviation is also observed for  $|\omega|$  in the range  $l/D = 0.2-0.6$  (figure 7a). In this range, the filament is not sufficiently long to affect the rotational behaviour of the sphere in a deterministic manner, but flow instability induced by the short filament may be critical.

During the fall, a wake region is generated behind the sphere, and the force exerted on the filament is affected by this wake. Lācis *et al.* (2014) assumed that the wake of a bluff body was a simple elliptical region for a fixed but rotatable 2-D cylinder with a rear-side filament in a uniform flow, and showed that the estimated fluid force acting on the filament was in good agreement with experimental results. Lācis *et al.* (2014, 2017) applied this assumption to a falling sphere with an elliptic plate. Similarly, we introduce a simplified wake with an elliptic shape (grey region in figure 8a) to account for the rotation mechanism of a sphere with a filament in terms of the centre of mass and the relative position of the filament to the wake. In addition to simplifying the wake shape, we also choose the size of the wake region arbitrarily to illustrate the relative position of the filament to the wake as the sphere rotates. The attachment of the filament means that the centre of mass of the entire model ( $\otimes$  symbol in figure 8a) is above the geometric centre of the sphere; the position of the centre of mass is exaggerated in the figure for clarity. To quantify the shift in the centre of mass by the attachment of the filament, the offset distance  $\gamma$  is defined as the distance between the geometric centre of the sphere and the centre of mass of the entire model. Although the value of  $\gamma$  is 0.2% of  $D$  for  $l/D = 1.0$  (the case exhibiting a

strong zigzag motion), it is sufficient to affect the rotational behaviour of the sphere (Will & Krug 2021*b*).

With the rotation of the sphere, a lift force  $F_L$  is generated in the direction normal to the tangential velocity  $v_t$  (figure 8*a*); in the figure, the reference frame is fixed with the sphere, and  $v_t$  is directed towards the sphere. The hydrodynamic force exerted on the filament is negligible compared with that on the sphere because the filament has significantly smaller surface area and volume. Therefore, only the force acting on the sphere is considered in this study. In analysing the force balance of the sphere perpendicular to its tangential velocity vector  $v_t$ , we define the lift force vector  $F_L$ . This vector encompasses all fluid-dynamic forces exerted on the sphere normal to  $v_t$ , including unsteady effects but excluding the hydrostatic (buoyancy) force. It can be acquired from the experimental data as follows:

$$F_L = \left( \frac{1}{6} \rho_s \pi D^3 \frac{dv_t}{dt} - F_{g,net} \right)_n = \frac{1}{6} \rho_s \pi D^3 \left[ \frac{dv_t}{dt} + \left( \frac{\rho_f}{\rho_s} - 1 \right) \mathbf{g} \right]_n. \quad (3.3)$$

The subscript  $n$  denotes the component in the direction normal to  $v_t$ , and  $F_{g,net}$  is the net gravitational force. In this study,  $F_L$  is determined by

$$F_L = \text{sgn} [\{F_L \times (-v_t)\} \cdot \mathbf{n}] |F_L|. \quad (3.4)$$

In (3.3) and (3.4),  $v_t$  is the tangential velocity of the sphere in the global reference frame.

Figures 8*b*) and 8*c*) present the angular velocity ratio  $\omega/|\omega_0|$  and lift force ratio  $F_L/|F_{L,0}|$  for  $l/D = 1.0$  and 2.0, respectively. As shown in figure 2*a*), the plain sphere exhibits slight horizontal displacements, and the time-averaged magnitude of the plain sphere's lift force,  $|F_{L,0}|$ , is non-zero, albeit small. The angular velocity  $\omega$  exhibits a similar temporal profile and period to the lift force  $F_L$  with a slight phase delay, implying that the rotation of the sphere is responsible for generating the lift force. This result is in agreement with the finding of Will & Krug (2021*b*), who reported that the angular velocity and the lift force are coupled for a plain falling sphere with significant angular velocity because of the shifted centre of mass. As the zigzag motion of the sphere becomes weaker (e.g.  $l/D = 2.0$ ), the magnitudes of  $\omega$  and  $F_L$  decrease. Although not presented here, the correlation between  $\omega$  and  $F_L$  is almost indistinguishable for  $l/D \leq 0.4$  and  $l/D \approx 3.0$ , where the degree of zigzag motion is very small (figure 3*b*).

Figure 8*a*) describes the fluid-dynamic forces and torques with respect to the centre of mass, allowing us to explain the rotational mechanism of the model in more detail. The drag force  $F_D$  acting on the sphere is parallel to the tangential velocity  $v_t$  and generates torque  $T_D$  in the direction that causes the filament to move away from the centreline, which is defined as the line parallel to the tangential velocity and passing through the sphere centre (vertical dashed line in figure 8*a*). By contrast, the flow outside the wake region generates a fluid force on the filament, resulting in torque  $T_{ext}$  in the direction towards the centreline. The portion of the filament outside the wake is illustrated as the blue line in figure 8*a*). The magnitude of the flow velocity (in the reference frame fixed with the sphere) outside the wake is much greater than that inside the wake, and the area outside the wake is located farther away from the centre of mass than the area inside the wake. Therefore, we focus on the torque generated by the flow outside the wake, which greatly exceeds the torque produced by the flow inside the wake.

As a sphere rotates in a certain direction, a lift force  $F_L$  normal to the tangential velocity is generated on the sphere. According to Will & Krug (2021*b*), in the case of a falling plain sphere where the centre of mass is positioned below its geometric centre, the torque induced by the lift force opposes the rotating direction of the sphere and suppresses its rotation. Consequently, no zigzag falling trajectory can be identified. By contrast, for a rising plain sphere with the centre of mass below the geometric centre, the external

flow in the reference frame fixed with the sphere acts in the opposite direction, so the lift-induced torque is generated in the rotating direction, enhancing the sphere's rotation, which eventually leads to a zigzag trajectory. That is, the centre of mass and the direction of external flow are important in determining the rotational dynamics and resulting trajectory of the plain sphere. For our model, where the centre of mass is positioned above the geometric centre of the sphere because of the filament, a lift-induced torque  $T_L$  is generated in the same direction as the rotation of the sphere, further strengthening its rotation (figure 8a).

The sphere with a strong zigzag motion undergoes periodic rotational oscillations, as demonstrated in figure 6 and supplementary movie 1(b). During the fall, the relative position of the filament to the wake region is shifted continuously by the rotation of the sphere. The positions of the filament with respect to the wake region were determined using dye visualisation experiments with fluorescein disodium salt. The visualised wake and filament were filmed by a high-speed camera (FASTCAM MINI-UX50, Photron, Inc.). The experimental trials were repeated to make the direction of maximum horizontal displacement nearly parallel to the field of view of the camera. Figure 9(a) and supplementary movie 2 present visualised wakes in sequence for  $l/D = 1.0$ , which produces a strong zigzag motion. In addition, the simplified schematics of the rotation process in the reference frame fixed with the sphere are illustrated in figure 9(b). The schematics are represented in two dimensions because the sphere rotation is dominant with respect to the axis normal to the trajectory plane for  $l/D = 1.0$ , and the incoming flow velocity  $v_t$  is expressed consistently in the upward direction for ease of comparison between the schematics.

A large portion of the filament is inside the wake when the filament is near the middle of the wake, i.e. when  $|\theta|$  is small (figure 9ai,bi). In this phase, the magnitudes of the angular velocity  $\omega$  and the lift force  $F_L$  are significant according to figures 8(b) and 8(c). The lift-induced torque  $T_L$  acts in the same direction as the drag-induced torque  $T_D$ , and the counter-torque produced by the external flow,  $T_{ext}$ , is small. As the sphere rotates with increasing  $\theta$ , the area of the filament exposed to the flow outside the wake becomes greater, leading to an increase in  $T_{ext}$ . Eventually,  $\theta$  reaches its maximum magnitude while  $\omega$  and  $F_L$  almost vanish (figure 9aai,bi). Thereafter, the sphere begins to rotate in the opposite direction because  $T_{ext}$  is still large, generating  $F_L$  in the opposite direction from the phase in figure 9(ai), and  $T_L$  aligns with the new rotation direction (figure 9aaii,bi);  $T_D$  does not change its direction before the filament returns to the centreline. As the filament moves to the other half of the wake region, reversing the sign of  $\theta$ , the directions of the lift force and torques are symmetric to those in the preceding half of the rotation process, and the sphere exhibits symmetric rotational behaviour (figure 9aiv–avi,biv–bvi).

As the filament extends from  $l/D = 1.0$ , the rotational motion of the sphere weakens as the average sphere angular velocity and maximum filament angle decrease (figure 7). Even when the filament is positioned near the middle of the wake, the area of the filament outside the wake becomes significant (figure 10). Consequently, the greater  $T_{ext}$  throughout the rotation process yields smaller values of  $|\omega|$  and  $|\theta|_{max}$ . Moreover, when  $l/D$  increases to 3.0, the moment of inertia of the model increases by 28.8% from that of  $l/D = 1.0$ , which plays a role in reducing the angular velocity. The less-pronounced rotation reduces the lift force acting on the sphere, leading to a weak zigzag motion.

Regarding shorter filaments ( $l/D < 0.8$ ), with which the degree of zigzag motion is very small (figure 3b), the filament does not cross to the other half of the wake region, in contrast to cases where the model exhibits symmetric rotational behaviour with a strong zigzag motion (e.g.  $l/D = 1.0$ ). Instead, the filament maintains a large  $\theta$  within the original half of the wake during the rotation process (figure 11). This asymmetric

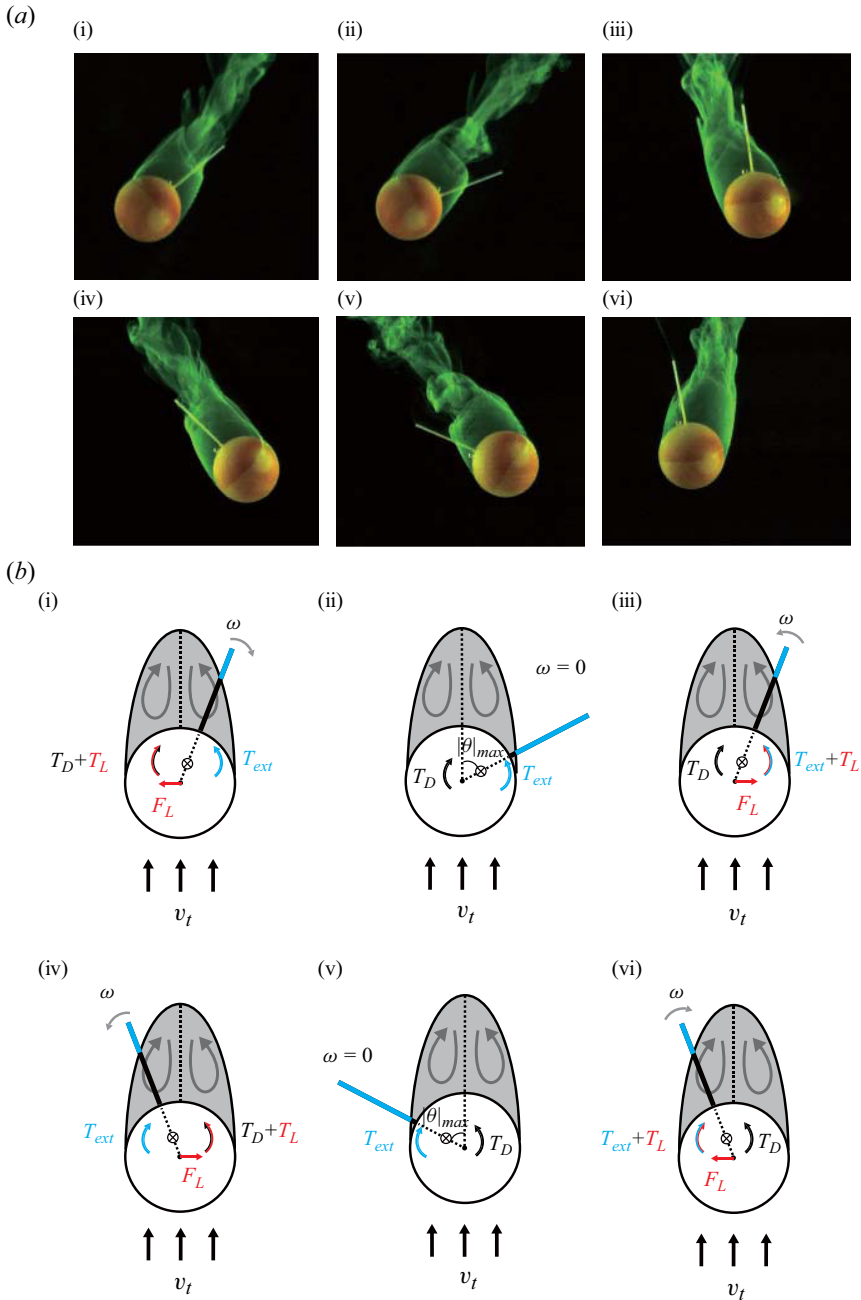


Figure 9. (a) Sequential snapshots of wake visualisation for  $l/D = 1.0$  with strong zigzag motion. (b) Corresponding simplified schematics illustrating the rotation process. For (a), see supplementary movie 2.

rotational behaviour results in a smaller  $|\overline{\omega}|$  compared with that for  $l/D = 1.0$  (figure 7a). In cases with symmetric rotational behaviour, the angular velocity of the sphere reaches its peak at approximately the time when the filament crosses the centreline ( $\theta = 0$ ) by virtue of  $T_{ext}$  being exerted in the prior half of the wake (figure 6a,b). However, for shorter

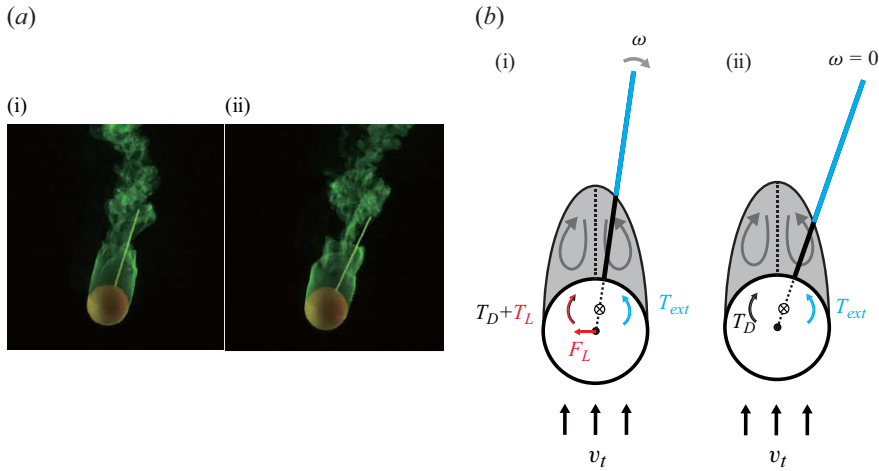


Figure 10. (a) Snapshots of wake visualisation for a long filament ( $l/D = 2.0$ ). (b) Corresponding simplified schematics of the rotation process.

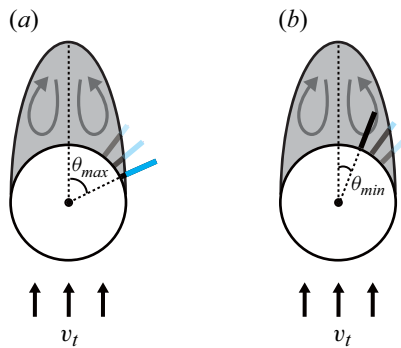


Figure 11. Simplified schematics of the rotation process for a short filament.

filaments,  $T_{ext}$  is minor, and the counter-torque, which is produced by the recirculating wake flow moving towards the rear side of the sphere in the middle of the wake region (grey arrows in figure 11), causes the filament to remain in one half of the wake, having a smaller  $|\omega|$ . Thus the zigzag motion, which basically requires symmetric rotation crossing the centreline, almost disappears.

Next, we evaluate the drag and lift coefficients of the sphere, and determine their trends in terms of the filament length. In previous studies of a falling or rising plain sphere, the drag coefficient of the sphere is defined based on its vertical velocity:  $C_{D,z} = 4D |\rho_s/\rho_f - 1| g / (3\bar{v}_z^2)$  (Jenny *et al.* 2004; Horowitz & Williamson 2010; Will & Krug 2021*a,b*). In this study, to include the effects of the tangential velocity directly, the drag and lift coefficients  $C_D$  and  $C_L$  are calculated using the tangential velocity of the sphere. The drag force vector  $F_D$ , which is the total fluid-dynamic force exerted on the sphere in the direction opposite to the tangential velocity vector in the global reference frame, is calculated based on the experimental data. The force balance equation is employed in a manner similar to the lift force  $F_L$  in (3.3):

$$F_D = \left( -\frac{1}{6} \rho_s \pi D^3 \frac{dv_t}{dt} + F_{g,net} \right)_t = \frac{1}{6} \rho_s \pi D^3 \left[ -\frac{dv_t}{dt} + \left( 1 - \frac{\rho_f}{\rho_s} \right) \mathbf{g} \right]_t. \quad (3.5)$$

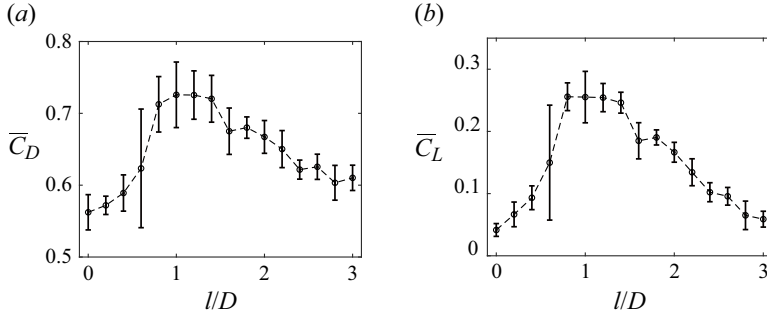


Figure 12. (a) Average drag coefficient  $\bar{C}_D$  and (b) average lift coefficient  $\bar{C}_L$  with respect to  $l/D$ .

The subscript  $t$  denotes the component parallel to  $\mathbf{v}_t$ . Then  $C_D$  and  $C_L$  are defined in the tangential and normal directions of the trajectory, respectively, and given as

$$C_D = \frac{2|\mathbf{F}_D|}{\rho_f v_t^2 \pi (D/2)^2} = \frac{4D \left| \frac{\rho_s}{\rho_f} \frac{d\mathbf{v}_t}{dt} + \left(1 - \frac{\rho_s}{\rho_f}\right) \mathbf{g} \right|_t}{3v_t^2}, \quad (3.6a)$$

$$C_L = \frac{2|\mathbf{F}_L|}{\rho_f v_t^2 \pi (D/2)^2} = \frac{4D \left| \frac{\rho_s}{\rho_f} \frac{d\mathbf{v}_t}{dt} + \left(1 - \frac{\rho_s}{\rho_f}\right) \mathbf{g} \right|_n}{3v_t^2}. \quad (3.6b)$$

Because  $C_D$  and  $C_L$  are derived from  $\mathbf{F}_D$  and  $\mathbf{F}_L$ , respectively, these coefficients also include the effects of unsteady fluid dynamics, rather than reflecting only quasi-steady forces.

When a sphere with a centre fixed in space is placed in a uniform flow, its rotation with respect to an axis transverse to the flow affects the wake structure, resulting in greater drag and lift compared with a fixed sphere without rotation (Giacobello *et al.* 2009; Kim 2009; Poon *et al.* 2014). The sphere’s rotation deflects the wake in a direction determined by the cross-product of the angular velocity vector and the free-stream vector. As the angular velocity of the sphere increases, the drag and lift coefficients also increase due to changes in the flow structure. Similar trends are observed in our model. In figure 12, both  $C_D$  and  $C_L$  averaged over the trajectory length between  $z/D = 0$  and  $z/D = 26.9$  show similar trends to the average magnitude of angular velocity  $|\omega|/|\omega_0|$  presented in figure 7(a). Both  $\bar{C}_D$  and  $\bar{C}_L$  increase in accordance with an increase in the angular velocity. As discussed in § 3.1, the tangential velocity of a falling sphere with a filament is lower than that of a plain sphere, and its trajectory is longer because of the horizontal displacement associated with the zigzag motion. In the presence of the filament,  $C_D$  and  $C_L$  are enhanced owing to the rotation of the sphere, which eventually leads to the reduced tangential velocity and elongated trajectory, respectively.

### 3.3. Effects of shifted centre of mass and hydrodynamic interaction of a filament

The attachment of a filament to the sphere enhances rotational dynamics through two mechanisms: shift in the centre of mass for the entire model, and hydrodynamic interaction between the filament and surrounding fluid. In this subsection, we examine quantitatively how each mechanism influences the falling dynamics by employing two additional models (figure 13). In the experimental model discussed in §§ 3.1 and 3.2, the sphere’s centre of mass coincides with its geometric centre when no filament is attached. However, the

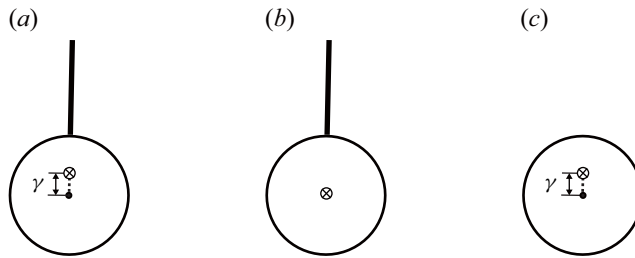


Figure 13. Schematics of the models with (a)  $l/D = 1.0$  and  $\gamma/D = 0.2\%$ , (b)  $l/D = 1.0$  and  $\gamma/D = 0$ , and (c)  $l/D = 0$  and  $\gamma/D = 0.2\%$ . The geometric centre of the sphere and the centre of mass of the entire model are denoted by  $\bullet$  and  $\otimes$ , respectively.

attachment of a filament shifts the centre of mass of the entire model above the geometric centre of the sphere (figure 13a). For example, with a filament of length ratio  $l/D = 1.0$ , the dimensionless offset distance  $\gamma/D$  is 0.2%.

To separate the effects of the shifted centre of mass and the hydrodynamic interaction of the filament, we designed an additional experimental model, in which the centre of mass of the entire model coincides with the geometric centre of the sphere when a filament is attached (figure 13b). To achieve zero offset distance between the centre of mass and the geometric centre ( $\gamma/D = 0$ ), the centre of mass of a sphere is positioned below the geometric centre by modifying its internal configuration. The offset distance of this sphere was calculated to ensure that the magnitude of this initial downward offset precisely matched the upward shift that would occur upon filament attachment. As a result, when the filament is attached to this sphere, the centre of mass of the entire model coincides with the geometric centre of the sphere.

Experimental results of the models with and without a shifted centre of mass are compared, focusing on a fixed filament length ratio  $l/D = 1.0$ , where a strong zigzag motion is observed. For comparison, the results of the model without a shifted centre of mass ( $\gamma/D = 0$ , figure 13b) are made dimensionless using those of the model with a shifted centre of mass ( $\gamma/D = 0.2\%$ , figure 13a), which is discussed in §§ 3.1 and 3.2 (table 1). In the table, the parameters denoted with subscript 1 refer to those of the model with  $l/D = 1.0$  and  $\gamma/D = 0.2\%$ . For the model with  $\gamma/D = 0$ , zigzag motion becomes weaker than in the model with  $\gamma/D = 0.2\%$ . Specifically, when  $\gamma/D$  changes from 0.2% to 0, the degree of zigzag motion decreases, having  $w^*/w_1^* = 0.73$ . In addition to the weakened zigzag motion, the lift force generated by the sphere merely affects the rotation of the sphere due to zero offset distance. Consequently, the sphere rotation is mitigated, as indicated by the average magnitude ratio of angular velocity  $|\overline{\omega}|/|\overline{\omega}_1| = 0.76$  and the maximum filament angle ratio  $|\theta|_{max}/|\theta|_{max,1} = 0.49$ : slower angular velocity and a narrower range of rotation. The reduced rotational dynamics also influences the translational dynamics, albeit in a minor way. With the change in  $\gamma/D$  from 0.2% to 0, the ratios of the average tangential velocity, trajectory length and falling time are  $\bar{v}_t/\bar{v}_{t,1} = 1.04$ ,  $L/L_1 = 0.99$  and  $t/t_1 = 0.95$ , respectively.

To examine the effects of the hydrodynamic interaction of the filament, we manufactured another experimental model (figure 13c), a plain sphere with the same offset distance ( $\gamma/D = 0.2\%$ ) as the model with  $l/D = 1.0$  in figure 13(a), by adjusting the internal configuration of the sphere. The results for the plain sphere with a shifted centre of mass ( $l/D = 0$ ,  $\gamma/D = 0.2\%$ ) are presented in dimensionless form, using those of the model with  $l/D = 1.0$  and  $\gamma/D = 0.2\%$  (table 1). When the model is influenced solely by the shifted centre of mass without the hydrodynamic interaction of the filament, the zigzag

Experimental model	$w^*/w_1^*$	$ \overline{\omega} / \overline{\omega}_1 $	$ \theta _{max}/ \theta _{max,1}$	$\bar{v}_t/\bar{v}_{t,1}$	$L/L_1$	$t/t_1$
(i) $l/D = 1.0$ and $\gamma/D = 0$	0.73	0.76	0.49	1.04	0.99	0.95
(ii) $l/D = 0$ and $\gamma/D = 0.2\%$	0.19	0.29	–	1.19	0.96	0.81

Table 1. Degree of zigzag motion  $w^*$ , average magnitude of sphere angular velocity  $|\overline{\omega}|$ , maximum magnitude of filament angle  $|\theta|_{max}$ , average tangential velocity  $\bar{v}_t$ , trajectory length  $L$ , and falling time  $t$  for two models with different configurations: (i)  $l/D = 1.0$  and  $\gamma/D = 0$ ; (ii)  $l/D = 0$  and  $\gamma/D = 0.2\%$ . The models of (i) and (ii) correspond to those in figures 13(b) and 13(c), respectively. The subscript 1 denotes the result of the model with  $l/D = 1.0$  and  $\gamma/D = 0.2\%$  in figure 13(a).

motion becomes weaker, and the rotational dynamics is significantly reduced compared to the model experiencing both effects. Notably, the mitigation of the zigzag motion and the reduction in the rotational dynamics is more pronounced than the model with  $l/D = 1.0$  and  $\gamma/D = 0$  corresponding to figure 13(b). For  $l/D = 0$  and  $\gamma/D = 0.2\%$ ,  $w^*/w_1^* = 0.19$  and  $|\overline{\omega}|/|\overline{\omega}_1| = 0.29$ , whereas these values are significantly higher at 0.73 and 0.76, respectively, for  $l/D = 1.0$  and  $\gamma/D = 0$ . Consequently, in the absence of the filament, changes in  $\bar{v}_t$ ,  $L$  and  $t$  are greater:  $\bar{v}_t/\bar{v}_{t,1}$ ,  $L/L_1$  and  $t/t_1$  for  $l/D = 0$  and  $\gamma/D = 0.2\%$  are 1.19, 0.96 and 0.81, respectively, while they are 1.04, 0.99 and 0.95 for  $l/D = 1.0$  and  $\gamma/D = 0$ . In summary, these results hint that for the model considered in §§ 3.1 and 3.2, the hydrodynamic interaction of the filament has a more substantial influence on the sphere’s falling dynamics than the shifted centre of mass, under the condition of a strong zigzag motion (e.g.  $l/D = 1.0$ ).

### 3.4. Change in sphere density

The effects of the filament length on the translational and rotational dynamics of the sphere have been discussed in the preceding subsections, with the sphere density remaining constant at  $\rho_s/\rho_f = 1.06$ . As the sphere becomes heavier, it is expected that the tangential velocity of the model will increase, affecting its rotational motion. In this subsection, we compare the falling dynamics of the model for higher density ratios. Preliminary experiments with spheres lighter than  $\rho_s/\rho_f = 1.06$  yielded significantly scattered results due to their proximity to neutral buoyancy. Therefore, this section focuses on the effects of increased sphere density. We first examine the dynamics of a sphere with a higher density ratio  $\rho_s/\rho_f = 1.12$  with respect to filament length  $l/D$ , and compare the results with those for a sphere at  $\rho_s/\rho_f = 1.06$ . Additionally, to comprehensively understand the effects of sphere density over a broader range, several cases with density ratios exceeding  $\rho_s/\rho_f = 1.12$  are investigated while maintaining the filament length constant at  $l/D = 1.0$ , where a strong zigzag motion is observed. As stated in § 2, the dimensionless moment of inertia  $I^*$  ( $= I_s/I_\Gamma$ ) remains very similar between the spheres with different  $\rho_s/\rho_f$  values ( $I^* \approx 0.96$ ), and the filament properties remain unchanged.

Regardless of sphere density, the centre of mass of the model is positioned above the geometric centre of the sphere due to the attached filament. The rotational mechanism described in § 3.2 also applies to the model with the greater density. Thus the model with  $\rho_s/\rho_f = 1.12$  exhibits a zigzag falling trajectory, similar to the model with  $\rho_s/\rho_f = 1.06$ . For both density ratios, the degree of zigzag motion  $w^*$  exhibits quite similar trends with respect to  $l/D$  (figure 14a). As the sphere density increases, its velocity also increases. In the reference frame fixed to the sphere, the velocity of the flow surrounding the sphere becomes greater for the heavier sphere. Consequently, the effects of  $T_{ext}$  are amplified, resulting in greater magnitudes of the angular velocity and lift force. Because of the

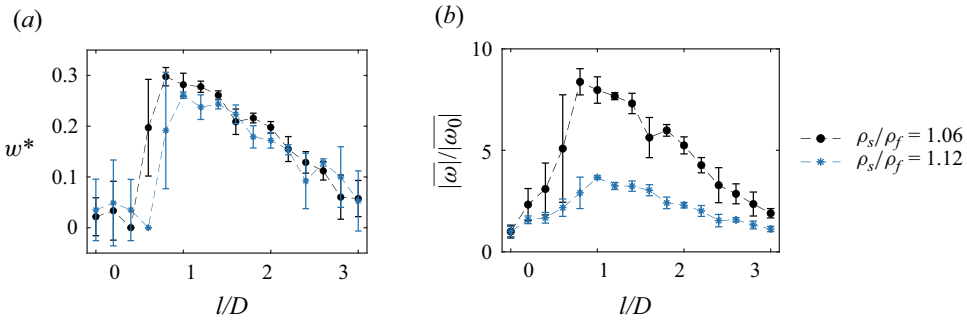


Figure 14. (a) Degree of zigzag motion  $w^*$ , and (b) average magnitude of sphere angular velocity  $|\omega|/|\omega_0|$ , for  $\rho_s/\rho_f = 1.06$  (black) and  $\rho_s/\rho_f = 1.12$  (blue). Here,  $I^* = 0.967$  for  $\rho_s/\rho_f = 1.06$ , and  $I^* = 0.959$  for  $\rho_s/\rho_f = 1.12$ .

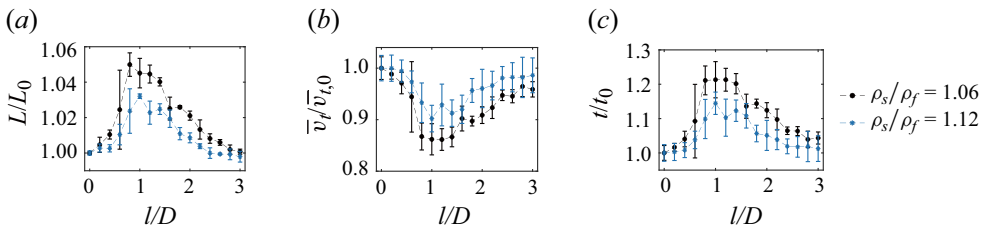


Figure 15. (a) Trajectory length  $L/L_0$ , (b) average tangential velocity  $\bar{v}_t/\bar{v}_{t,0}$ , and (c) falling time  $t/t_0$ , for  $\rho_s/\rho_f = 1.06$  (black) and  $\rho_s/\rho_f = 1.12$  (blue).

enhanced lift force, the magnitudes of the horizontal displacement and the degree of zigzag motion appear to be comparable between the two density ratios in the entire range of  $l/D$ , although the heavier sphere falls faster; strictly,  $w^*$  for  $\rho_s/\rho_f = 1.12$  is slightly smaller than that for  $\rho_s/\rho_f = 1.06$  near  $l/D = 1.0$  with the strong zigzag motion.

For the heavier sphere, the centre of mass of the model is located closer to the geometric centre of the sphere. This reduced offset distance annihilates the torques induced by the shifted centre of mass. Figure 14(b) compares the average magnitude of the sphere's angular velocity  $|\omega|$  divided by that of the plain sphere  $|\omega_0|$  with the same density for the two cases. In this subsection, results denoted with subscript 0 refer to those of the plain sphere with the same density as the sphere in the numerator of the dimensionless quantities. Although the dimensional  $|\omega|$  of  $\rho_s/\rho_f = 1.12$  significantly exceeds that of  $\rho_s/\rho_f = 1.06$  across all  $l/D$  values, the dimensionless  $|\omega|/|\omega_0|$  of  $\rho_s/\rho_f = 1.12$  is less than that of  $\rho_s/\rho_f = 1.06$ , indicating that the filament has less impact on the rotational dynamics for the heavier sphere. For example, at  $l/D = 1.0$ ,  $|\omega|/|\omega_0| = 3.7$  for  $\rho_s/\rho_f = 1.12$ , while  $|\omega|/|\omega_0| = 8.0$  for  $\rho_s/\rho_f = 1.06$ .

In addition to the rotational dynamics, the translational dynamics is less affected by the filament in the case of the heavier sphere. Figures 15(a) and 15(b) present the dimensionless trajectory length  $L/L_0$  and average tangential velocity  $\bar{v}_t/\bar{v}_{t,0}$ , respectively, for different density ratios. Both  $L/L_0$  and  $\bar{v}_t/\bar{v}_{t,0}$  exhibit similar trends with respect to  $l/D$ , regardless of the sphere density. The dimensional trajectory length  $L$  is similar for both density ratios across the entire range of  $l/D$ . However, the dimensionless  $L/L_0$  is smaller for the sphere with  $\rho_s/\rho_f = 1.12$ . In terms of a dimensional quantity, the average tangential velocity  $\bar{v}_t$  of the heavier sphere is significantly greater than that of the lighter

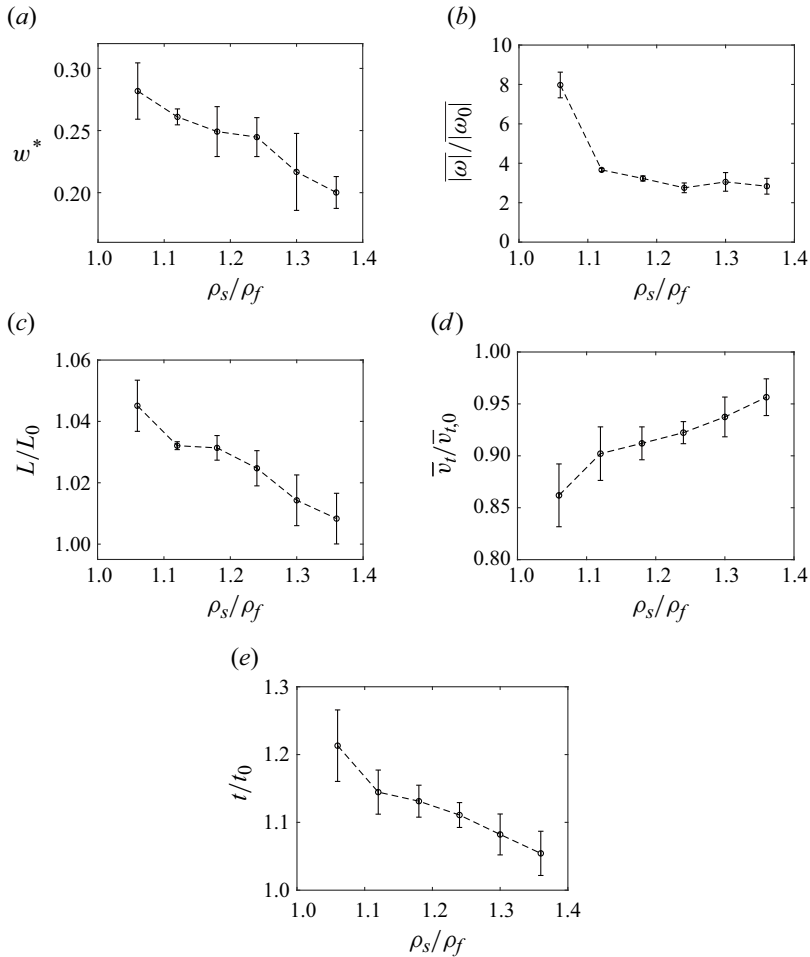


Figure 16. (a) Degree of zigzag motion  $w^*$ , (b) average magnitude of angular velocity  $|\omega|/|\omega_0|$ , (c) trajectory length  $L/L_0$ , (d) average tangential velocity  $\bar{v}_t/\bar{v}_{t,0}$ , and (e) falling time  $t/t_0$ , with respect to  $\rho_s/\rho_f$  for the spheres with  $l/D = 1.0$ . Here,  $I^* \approx 0.96$  for all cases.

sphere for all  $l/D$ . Moreover, the dimensionless  $\bar{v}_t/\bar{v}_{t,0}$  with  $\rho_s/\rho_f = 1.12$  exhibits a greater magnitude than that of  $\rho_s/\rho_f = 1.06$ . The smaller  $L/L_0$  and greater  $\bar{v}_t/\bar{v}_{t,0}$  reduce the dimensionless falling time  $t/t_0$  for the heavier sphere (figure 15c).

To further examine the effects of sphere density ratios greater than  $\rho_s/\rho_f = 1.12$ , the spheres with four different density ratios,  $\rho_s/\rho_f = 1.18, 1.24, 1.30, 1.36$ , were manufactured additionally by modifying the internal configurations of the spheres. Similar to the aforementioned results between  $\rho_s/\rho_f = 1.06$  and  $\rho_s/\rho_f = 1.12$ , for the spheres with  $\rho_s/\rho_f > 1.12$ , increasing density further reduces the influence of the filament on the falling dynamics because the offset distance between the centre of mass of the entire model and the geometric centre of the sphere becomes smaller. As the sphere density increases, the zigzag motion gradually weakens, and  $w^*$  decreases monotonically (figure 16a). This reduction in the zigzag motion correlates with a decrease in  $|\omega|/|\omega_0|$  (figure 16b). Consequently, with increasing sphere density, the differences in translational dynamics between a sphere with a filament and a plain sphere of the same density become less pronounced. Specifically, both the dimensionless trajectory length  $L/L_0$  and the

dimensionless average tangential velocity  $\bar{v}_t/\bar{v}_{t,0}$  approach unity as the sphere density increases (figures 16c,d). This convergence leads to the shorter dimensionless falling time  $t/t_0$  for the heavier sphere (figure 16e). In summary, regarding the dimensionless parameters, the rotational motion of the sphere with the higher density is less distinct than for the lower-density sphere due to the smaller offset distance between the centre of mass and the geometric centre. This change mitigates the effects of the filament on the translational motion.

#### 4. Concluding remarks

In this study, we have experimentally investigated the role of a filament-type appendage on the falling dynamics of a sphere by varying the filament length and sphere density. The sphere, which falls vertically in the absence of the filament, exhibits a distinctive zigzag trajectory and periodic rotation when a filament is attached to its rear side. The sphere falls more slowly as the degree of zigzag motion becomes greater because of the extended path length and the reduction in tangential velocity. A strong zigzag motion is accompanied by enhanced rotational dynamics. The rotation mechanism of the sphere according to the filament length was determined in terms of the location of the centre of mass and the relative position between the filament and the wake region. The coupling between the translational and rotational dynamics of the sphere was identified through the correlation between the angular velocity and the fluid force coefficients. As the sphere density increases, the centre of mass shifts closer to the geometric centre of the sphere, annihilating the effects of the filament on the falling dynamics.

Although experimental measurements of flow velocity are required in order to examine the associated effects on fluid forces and torques, this would be challenging for a freely falling sphere. Thus our analysis of the flow surrounding the sphere has been limited to qualitative observations. Nevertheless, this study has identified the zigzag falling motion that is rarely observed in plain spheres, and has revealed the rotational mechanism induced by the interaction between the filament and the surrounding fluid, which is essential in elucidating the complicated falling behaviours. Following this experimental study, numerical simulations would permit the quantitative analysis of the distribution of the flow surrounding a falling sphere. Regarding applications, by virtue of the zigzag motion and increased falling time, a filament-type appendage may be adopted as a strategy for enhancing the dispersion of bluff objects under the presence of external flows.

**Supplementary movies.** Supplementary movies are available at <https://doi.org/10.1017/jfm.2025.271>.

**Funding.** This work was supported by the National Research Foundation of Korea (NRF) grant funded by the Korea government (MSIT) (RS-2024-00355146).

**Declaration of interests.** The authors report no conflict of interest.

#### Appendix A. Procedure and validation of orientation measurement

The orientation measurement in this study follows the method described by Mathai *et al.* (2016). In this method, the orientation of the sphere is determined by analysing the filmed image of a pattern on the sphere's surface. The measured orientation represents how the sphere has rotated from a predetermined reference orientation. This rotation is expressed using the axis-angle notation as  $\mathbf{q} = (k_x, k_y, k_z, \alpha)$ , where  $(k_x, k_y, k_z)$  is the direction of the axis of rotation and  $\alpha$  is the angle of rotation with respect to the axis. The reference orientation is defined as  $\mathbf{q}_0 = (1, 0, 0, 0)$ .

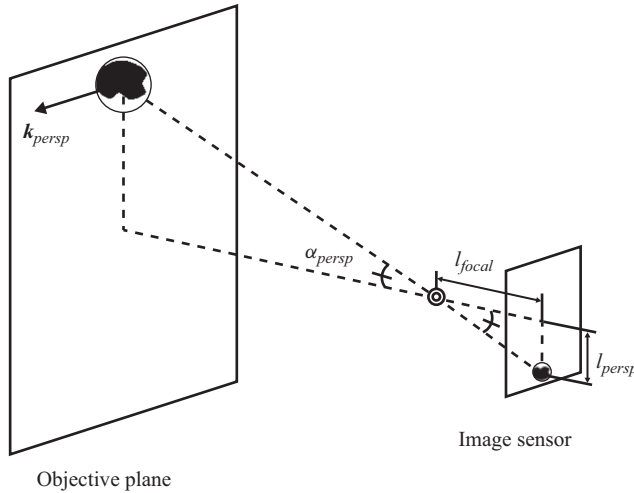


Figure 17. Schematic of perspective projection geometry for an objective plane and an image sensor. The  $\odot$  symbol represents the focal point of the camera.

When the position of the sphere in the captured image deviates from the image centre, the measured orientation  $\mathbf{q}$  is slightly rotated due to perspective distortion. To correct for this distortion and accurately calculate the orientation in the global reference frame,  $\mathbf{q}_{abs}$ , a correction based on the method of Zimmermann (2012), was applied (figure 17). Specifically,  $\mathbf{q}$  is rotated by an angle  $\alpha_{persp}$ , which is the angle between the vector from the camera’s focal point to the centre of an objective plane and the vector from the focal point to the sphere. The measured orientation  $\mathbf{q}$  is first converted into a rotation matrix  $\mathbf{R}$  using Rodrigues’ rotation formula. Next, the perspective distortion angle  $\alpha_{persp}$  is calculated as  $\alpha_{persp} = \arctan(l_{persp}/l_{focal})$ , where  $l_{persp}$  and  $l_{focal}$  represent the distance from the image centre to the sphere centre on an image sensor, and the focal length of the camera, respectively. The corresponding rotation matrix  $\mathbf{R}_{persp}$  is constructed. For  $\mathbf{R}_{persp}$ , the axis of rotation is defined as the vector parallel to the objective plane and perpendicular to the line connecting the focal point to the sphere centre. To correct for the perspective distortion,  $\mathbf{R}$  is multiplied by the transpose of  $\mathbf{R}_{persp}$ , yielding  $\mathbf{R}_{abs} = \mathbf{R}_{persp}^T \mathbf{R}$ . Finally, the orientation without perspective distortion,  $\mathbf{q}_{abs}$ , is then derived from  $\mathbf{R}_{abs}$ .

To validate the accuracy of the measured orientation angles, the sphere was rotated by a predetermined angle  $\Delta\alpha_{pre}$ , and the measured angle difference between the initial and final orientations of the sphere was compared with the predetermined angle. The sphere with the pattern, which was fixed in translation but freely rotatable with respect to a vertical axis, was rotated by  $\Delta\alpha_{pre} = 10^\circ, 20^\circ, 30^\circ, 40^\circ, 50^\circ, 60^\circ$  from the initial random orientation. The camera filmed the sphere before and after the rotation at 250 frames per second for 0.4 s each, and the time-averaged initial and final orientations of the sphere,  $\bar{\mathbf{q}}_i$  and  $\bar{\mathbf{q}}_f$ , were measured from the captured images. To calculate the angle difference, the initial and final orientations,  $\bar{\mathbf{q}}_i$  and  $\bar{\mathbf{q}}_f$ , were first converted to rotation matrices  $\mathbf{R}_i$  and  $\mathbf{R}_f$ , respectively, using the Rodrigues’ rotation formula. These rotational matrices were then corrected as  $\mathbf{R}_{i,abs}$  and  $\mathbf{R}_{f,abs}$ . The measured angle difference  $\Delta\alpha_{exp}$  between  $\bar{\mathbf{q}}_{i,abs}$  and  $\bar{\mathbf{q}}_{f,abs}$  was then obtained by calculating the matrix  $\mathbf{R}_\Delta = \mathbf{R}_{i,abs}^T \mathbf{R}_{f,abs}$ . Finally,  $\mathbf{R}_\Delta$  was converted to the axis-angle notation  $\mathbf{q}_\Delta = (k_{\Delta x}, k_{\Delta y}, k_{\Delta z}, \Delta\alpha_{exp})$ , yielding  $\Delta\alpha_{exp}$ , where  $k_{\Delta x}$ ,  $k_{\Delta y}$ , and  $k_{\Delta z}$  are the  $x$ -,  $y$ - and  $z$ -components of the axis of rotation from  $\bar{\mathbf{q}}_{i,abs}$  to  $\bar{\mathbf{q}}_{f,abs}$ . The values of  $\Delta\alpha_{exp}$  are almost identical to those of the predetermined angle

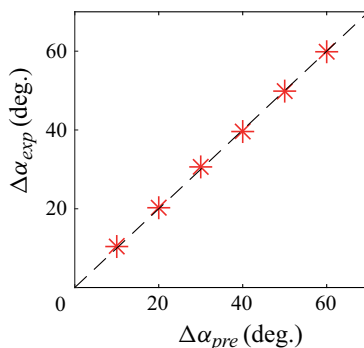


Figure 18. Measured angle difference  $\Delta\alpha_{exp}$  between the initial and final orientations of the fixed but rotatable sphere versus predetermined angle difference  $\Delta\alpha_{pre}$ . The sphere rotates with respect to a vertical axis in the validation experiment.

$\Delta\alpha_{pre}$  (figure 18), with maximum error less than  $1^\circ$ . This indicates that the method used to measure the orientation of the sphere is sufficiently reliable for analysing the sphere's rotational dynamics.

## REFERENCES

- ABDI, R., REZAZADEH, N. & ABDI, M. 2019 Investigation of passive oscillations of flexible splitter plates attached to a circular cylinder. *J. Fluids Struct.* **84**, 302–317.
- ANDERSON, E.A. & SZEWCZYK, A.A. 1997 Effects of a splitter plate on the near wake of a circular cylinder in 2 and 3-dimensional flow configurations. *Exp. Fluids* **23** (2), 161–174.
- APELT, C.J., WEST, G.S. & SZEWCZYK, A.A. 1973 The effects of wake splitter plates on the flow past a circular cylinder in the range  $104 < Re < 5 \times 104$ . *J. Fluid Mech.* **61** (1), 187–198.
- ASSEN, M.P., WILL, J.B., NG, C.S., LOHSE, D., VERZICCO, R. & KRUG, D. 2024 Rising and settling 2-D cylinders with centre-of-mass offset. *J. Fluid Mech.* **981**, A7.
- BAGHERI, S., MAZZINO, A. & BOTTARO, A. 2012 Spontaneous symmetry breaking of a hinged flapping filament generates lift. *Phys. Rev. Lett.* **109** (15), 154502.
- BAO, Y. & TAO, J. 2013 The passive control of wake flow behind a circular cylinder by parallel dual plates. *J. Fluids Struct.* **37**, 201–219.
- ERN, P., RISSO, F., FABRE, D. & MAGNAUDET, J. 2012 Wake-induced oscillatory paths of bodies freely rising or falling in fluids. *Annu. Rev. Fluid Mech.* **44** (1), 97–121.
- FAVIER, J., DAUPTAIN, A., BASSO, D. & BOTTARO, A. 2009 Passive separation control using a self-adaptive hairy coating. *J. Fluid Mech.* **627**, 451–483.
- GERRARD, J.H. 1966 The mechanics of the formation region of vortices behind bluff bodies. *J. Fluid Mech.* **25** (2), 401–413.
- GIACOBELLO, M., OOI, A. & BALACHANDAR, S. 2009 Wake structure of a transversely rotating sphere at moderate Reynolds numbers. *J. Fluid Mech.* **621**, 103–130.
- HEDRICK, T.L. 2008 Software techniques for two- and three-dimensional kinematic measurements of biological and biomimetic systems. *Bioinspir. Biomim.* **3** (3), 034001.
- HOROWITZ, M. & WILLIAMSON, C.H.K. 2010 The effect of Reynolds number on the dynamics and wakes of freely rising and falling spheres. *J. Fluid Mech.* **651**, 251–294.
- JENNY, M., DUŠEK, J. & BOUCHET, G. 2004 Instabilities and transition of a sphere falling or ascending freely in a Newtonian fluid. *J. Fluid Mech.* **508**, 201–239.
- KIM, D. 2009 Laminar flow past a sphere rotating in the transverse direction. *J. Mech. Sci. Technol.* **23** (2), 578–589.
- KWON, K. & CHOI, H. 1996 Control of laminar vortex shedding behind a circular cylinder using splitter plates. *Phys. Fluids* **8** (2), 479–486.
- LĀCIS, U., BROSE, N., INGREMEAU, F., MAZZINO, A., LUNDELL, F., KELLAY, H. & BAGHERI, S. 2014 Passive appendages generate drift through symmetry breaking. *Nat. Commun.* **5** (1), 1–9.
- LĀCIS, U., OLIVIERI, S., MAZZINO, A. & BAGHERI, S. 2017 Passive control of a falling sphere by elliptic-shaped appendages. *Phys. Rev. Fluids* **2** (3), 033901.

- LEE, J. & YOU, D. 2013 Study of vortex-shedding-induced vibration of a flexible splitter plate behind a cylinder. *Phys. Fluids* **25** (11), 110811.
- LEE, M., LEE, S.H. & KIM, D. 2020 Stabilized motion of a freely falling bristled disk. *Phys. Fluids* **32** (11), 113604.
- MAO, Q., LIU, Y. & SUNG, H.J. 2022a Drag reduction by flapping a flexible filament behind a stationary cylinder. *Phys. Fluids* **34** (8), 087123.
- MAO, Q., ZHAO, J., LIU, Y. & SUNG, H.J. 2022b Drag reduction by a flexible hairy coating. *J. Fluid Mech.* **946**, A5.
- MATHAI, V., NEUT, M.W.M., VAN DER POEL, E.P. & SUN, C. 2016 Translational and rotational dynamics of a large buoyant sphere in turbulence. *Exp. Fluids* **57** (4), 1–10.
- MATHAI, V., ZHU, X., SUN, C. & LOHSE, D. 2017 Mass and moment of inertia govern the transition in the dynamics and wakes of freely rising and falling cylinders. *Phys. Rev. Lett.* **119** (5), 054501.
- NIU, J. & HU, D.L. 2011 Drag reduction of a hairy disk. *Phys. Fluids* **23** (10), 101701.
- PARK, H., BAE, K., LEE, B., JEON, W.P. & CHOI, H. 2010 Aerodynamic performance of a gliding swallowtail butterfly wing model. *Exp. Fluids* **50** (9), 1313–1321.
- POON, E.K., OOI, A.S., GIACOBELLO, M., IACCARINO, G. & CHUNG, D. 2014 Flow past a transversely rotating sphere at Reynolds numbers above the laminar regime. *J. Fluid Mech.* **759**, 751–781.
- QIU, Y., SUN, Y., WU, Y. & TAMURA, Y. 2014 Effects of splitter plates and Reynolds number on the aerodynamic loads acting on a circular cylinder. *J. Wind Engng Ind. Aerodyn.* **127**, 40–50.
- ROSHKO, A. 1955 On the wake and drag of bluff bodies. *J. Aeronaut. Sci.* **22** (2), 124–132.
- SHUKLA, S., GOVARDHAN, R.N. & ARAKERI, J.H. 2023 Flow over a circular cylinder with a flexible splitter plate. *J. Fluid Mech.* **973**, A19.
- VELDHUIS, C.H.J. & BIESHEUVEL, A. 2007 An experimental study of the regimes of motion of spheres falling or ascending freely in a Newtonian fluid. *Intl J. Multiphase Flow* **33** (10), 1074–1087.
- WILL, J.B. & KRUG, D. 2021a Dynamics of freely rising spheres: the effect of moment of inertia. *J. Fluid Mech.* **927**, A7.
- WILL, J.B. & KRUG, D. 2021b Rising and sinking in resonance: mass distribution critically affects buoyancy-driven spheres via rotational dynamics. *Phys. Rev. Lett.* **126** (17), 174502.
- WU, J., QIU, Y.L., SHU, C. & ZHAO, N. 2014 Flow control of a circular cylinder by using an attached flexible filament. *Phys. Fluids* **26** (10), 103601.
- ZIMMERMANN, R. 2012 How large spheres spin and move in turbulent flows. PhD thesis, Ecole normale supérieure de Lyon–ENS LYON, France.
- ZIMMERMANN, R., GASTEUIL, Y., BOURGOIN, M., VOLK, R., PUMIR, A. & PINTON, J.F. 2011 Tracking the dynamics of translation and absolute orientation of a sphere in a turbulent flow. *Rev. Sci. Instrum.* **82** (3), 033906.